C. J. Lissenden
Engineering Science and Mechanics,
Penn State,
University Park, PA 16801

S. Choi
Engineering Science and Mechanics,
Penn State,
University Park, PA 16801

H. Cho
Engineering Science and Mechanics,
Penn State,
University Park, PA 16801

A. Motta
Mechanical and Nuclear Engineering,
Penn State,
University Park, PA 16801

K. Hartig
Mechanical and Nuclear Engineering,
Penn State,
University Park, PA 16801

X. Xiao
Mechanical and Nuclear Engineering,
Penn State,
University Park, PA 16801

S. Le Berre
Mechanical and Nuclear Engineering,
Penn State,
University Park, PA 16801

S. Brennan
Mechanical and Nuclear Engineering,
Penn State,
University Park, PA 16801

K. Reichard
Applied Research Laboratory,
Penn State,
University Park, PA 16801

R. Leary
Mechanical and Nuclear Engineering,
Penn State,
University Park, PA 16801

B. McNelly
Mechanical and Nuclear Engineering,
Penn State,
University Park, PA 16801

I. Jovanovic
Mechanical and Nuclear Engineering,
Penn State,
University Park, PA 16801;
Nuclear Engineering and Radiological Sciences,
University of Michigan,
Ann Arbor, MI 48109

Toward Robotic Inspection of Dry Storage Casks for Spent Nuclear Fuel

Extended dry storage of spent nuclear fuel makes it desirable to assess the structural integrity of the storage canisters. Stress corrosion cracking of the stainless steel canister is a potential degradation mode especially in marine environments. Sensing technologies are being developed with the aim of detecting the presence of chloride-bearing salts on the surface of the canister as well as whether cracks exist. Laser-induced breakdown spectroscopy (LIBS) methods for the detection of Chlorine are presented. In addition, ultrasonic-guided wave detection of crack-like notches oriented either parallel or perpendicular to the shear horizontal wave vector is demonstrated using the pulse-echo mode, which greatly simplifies the robotic delivery of the noncontact electromagnetic acoustic transducers (EMATs). Robotic delivery of both EMATs and the LIBS system is necessary due to the high temperature and radiation environment inside the cask where the measurements need to be made. Furthermore, the space to make the measurements is very constrained and maneuverability is confined by the geometry of the storage cask. In fact, a large portion of the canister surface is inaccessible due to the presence of guide channels on the inside of the cask's overpack, which is strong motivation for using guided waves for crack detection. Among the design requirements for the robotic system are to localize and track where sensor measurements are made to enable return to those locations, to avoid wedging or jamming of the robot, and to tolerate high temperatures and radiation levels. [DOI: 10.1115/1.4035788]

Contributed by the Pressure Vessel and Piping Division of ASME for publication in the JOURNAL OF PRESSURE VESSEL TECHNOLOGY. Manuscript received August 12, 2016; final manuscript received January 11, 2017; published online February 8, 2017. Assoc. Editor: Haofeng Chen.

Introduction

The fuel cycle is an integral part of nuclear power generation. Once the nuclear fuel is spent, the assemblies are removed from the reactor and placed in wet storage pools, which provide cooling. Eventually, the decay heat generation in the fuel assemblies is low enough that they can be taken out of wet storage and sealed in an inert environment inside dry storage casks before being transported to a repository for disposal.

In the absence of a final repository, the extended use of dry storage for spent nuclear fuel from U.S. nuclear power plants needs to be assessed to confirm the structural integrity of the storage casks. Structural integrity analysis entails (i) an intimate knowledge of potential failure modes, as well as the associated degradation processes, and (ii) nondestructive inspection. Because the canisters are encased in a concrete overpack, the access is limited and/or costly.

The goal of this paper is to report our recent research efforts toward robotic nondestructive inspection (NDI) of dry storage casks. The accomplishments presented herein form the basis for robotic inspection tools and methods currently being developed. This paper is organized as follows. The next section, Dry Storage of Spent Nuclear Fuel, describes dry storage casks, their features that make NDI challenging, and a possible degradation mode of concern. Then, a laser-induced breakdown spectroscopy (LIBS)-based method to sense salts on the surface of the stainless steel canister is described along with some initial laboratory results. Thereafter, compact electromagnetic acoustic transducers (EMATs) are discussed as a noncontact means to send and receive shear horizontal waves that are sensitive to stress corrosion cracking. To date, LIBS and EMAT measurements were made in the laboratory, with an eye toward setups that are advantageous for robotic delivery systems. The next section, Robotic Delivery System, describes sizing the robotic system to prevent it from wedging or jamming along the delivery path. Finally, conclusions are drawn regarding the design of the robotic inspection system.

Dry Storage of Spent Nuclear Fuel

When ready for dry storage, fuel assemblies in the cooling pool are loaded into the basket inside a welded cylindrical stainless steel canister that is roughly 2 m in diameter, 5 m long, and 15 mm thick. Once loaded, the lid is welded onto the canister and the canister is backfilled with helium. The canister is then transported to the independent spent fuel storage installation and placed inside an overpack for shielding, cooling, and protection. Overpacks vary considerably by vendor, but there are two basic types: vertical axis systems are thick-walled steel clad concrete cylinders concentric to the canister, and horizontal axis systems are cuboidal concrete boxes and have a steel frame to support the canister in a horizontal orientation. A photo of a vertical axis HI-STORM cask is shown in Fig. 1 since that is the focus of this paper. A cutaway rendering of a HI-STORM cask is shown in Fig. 2. Both cask types have a well-defined ventilation system to provide convective cooling of the canister; however, the gap between canister and overpack is on the order of 10 cm for vertical axis systems, while the plenum is quite spacious in horizontal axis systems. The environment inside the overpack is too harsh for humans due to high temperature and radiation (primarily gamma). Besides, vertical axis systems are far too constrained for human access. Thus, any inspection of a canister inside an overpack needs to be done with the assistance of a robotic system. The alternative of removing the canister from the overpack for inspection is costly and cumbersome.

Degradation of the overpack would most likely be associated with concrete degradation due to freeze-thaw or alkali-silica reaction. Scanning NDI methods related to this concern are reported elsewhere [1], but here the emphasis is on the canister. A potential degradation mode for canisters, especially those located in marine environments, is chloride-induced stress corrosion cracking [2–4]. Stress corrosion cracking (SCC) is a complex phenomenon that causes crack growth at a stress intensity factor lower than the plane strain fracture toughness K_{IC} and that manifests itself differently depending on the material, the type and level of loading, and the environment [5,6]. Some stainless steel alloys can be sensitized by high temperature excursions that deplete chromium at the grain boundaries. For instance, welding can create a heat-affected zone that becomes susceptible to SCC. Welding also creates thermal residual stresses, which in the case of canister welds are not stress relieved [4].

There are three conditions necessary for SCC to occur: the material is susceptible, existence of a tensile driving force, and

Fig. 1 Unloaded HI-STORM dry storage cask

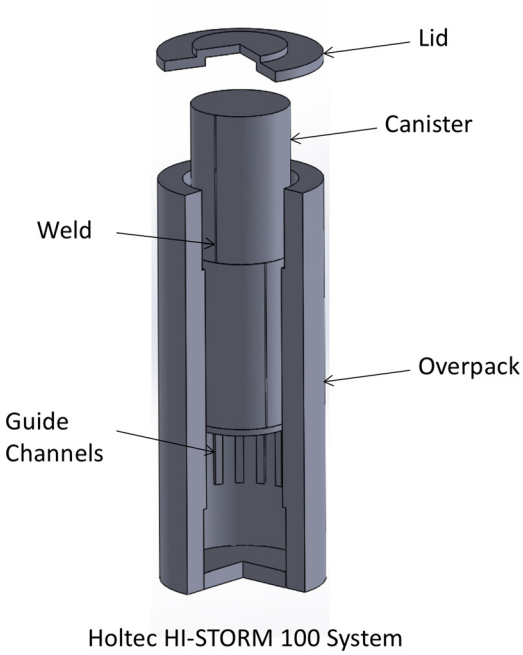

Fig. 2 Three-dimensional rendering of HI-STORM dry storage cask

the presence of a corrosive environment. The third, and critical, element is brought about in this case by the presence of chlorides in solution on the surface of the stainless steel. In a marine environment, it is possible that airborne salts containing chlorides enter the cask through the inlet vents with the cooling air and get deposited on the surface of the stainless steel canister. Under the right combination of temperature and humidity, the salt could deliquesce on the surface, thereby creating conditions whereby SCC could occur [6]. While crack initiation and growth is dependent upon all of the above factors, experience and expectations from modeling imply that cracks transverse to the weld or parallel to it are predisposed to occur in the heat-affected zone. Experience also shows that stress corrosion cracks in austenitic stainless steel are primarily intergranular and therefore contain significant branching [7]. We want to emphasize that these are educated expectations and do not want to discount the possibility of other degradation processes.

A robotic inspection system is being developed to use LIBS for surface composition measurements on the stainless steel canister. To make this practical, an optical fiber will be used to deliver the intense light from the laser to the surface and back to a spectrometer so that the laser and spectrometer can be located in a command center outside the cask. The robotic system will also deliver EMATs for crack detection using shear horizontal (SH) waves. One of the real advantages of using SH waves is that they do not require access to the entire surface of the canister. Some vertical axis overpack models have guide channels to maintain concentricity between the canister and the overpack that effectively block access to roughly half the canister surface. In these cask models, the robotic system is essentially constrained to move vertically between the guides. This is the design basis for our robotic inspection system. In addition to LIBS and EMAT measurements, the robotic inspection system is expected to measure temperature with thermocouples and ionizing radiation with a miniature Geiger Muller tube. The next section, Sensing Salt Deposits, describes LIBS measurements of salts on stainless steel.

Sensing Salt Deposits

As stated above, the presence of chlorine ions in solution on the surface of stainless steel, in conjunction with mechanical stress, can lead to stress corrosion cracking. Thus, it is of great interest to measure the salt concentration on the canister surface to ensure that the concentration of chlorine on the canister is not high enough to cause SCC. It has been reported that for the steels under consideration and in dry storage conditions, susceptibility to stress corrosion cracking can occur with concentrations as low as $0.8\,g/m^2$ [8]; we therefore set the range of interest for chlorine detection between 0.1 and $1\,g/m^2$. We chose to use laser-induced breakdown spectroscopy (LIBS) to conduct these measurements, primarily due to its compatibility with remote measurements in confined, hostile (high temperature and radiation) environments and its good elemental sensitivity [9].

LIBS involves focusing a pulsed laser onto the sample surface, generating ionized and excited particles in luminous plasma, and resolving emission lines from the plasma that are characteristic of the elements of interest [10,11]. LIBS has been widely used for its versatility, simplicity, and ability to perform in situ, rapid chemical analysis and has been extensively studied to improve its analytical performance by optimizing experimental parameters [10,11]. However, characterization of chlorine on stainless steel by LIBS is challenging due to the high excitation energy of chlorine of over 10 eV and the potential for interference from iron emission lines when the spectrometer resolution is limited [8,12].

Dual-pulse LIBS could greatly enhance the chlorine emission intensity [8,12]; however, such complex delivery configuration may not allow delivery of LIBS in the conditions of dry cask storage monitoring. Eto and Fujii [9] recently demonstrated a fiber-coupled LIBS system and a coaxial focusing configuration for the detection of chlorine on stainless steel in confined space. However, reliably detecting the chlorine emission line at 837.6 nm when chlorine is deposited on steel remains challenging, especially when quantitative concentration measurements are sought at low concentrations.

One possible alternative is to use the detection of Na to infer the presence of salt (and chlorine). This is justified in part by the fact that no significant variation of the ratio of alkali elements such as Na, Mg, and K to chlorine has been observed in oceans and major seas [13]. Considering the fact that alkali metals could be readily measured by LIBS with a typical limit of detection of a few ppm, they could serve as surrogates for the measurement of total chlorine concentration [14]. This assumes that no environmental speciation of Cl and Na occurs. For preliminary measurements, samples with homogeneous distribution of NaCl on stainless steel have been created and the ability to detect and quantify the Na emission line in LIBS measurement with an scanning electron microscopy (SEM)/energy dispersive x-ray spectrometry (EDS) benchmark has been demonstrated.

Figure 3 shows the experimental setup for LIBS measurements. A Q-switched Nd:YAG laser (spectra physics quanta-ray) with pulse duration of 10 ns and a repetition rate of 10 Hz was operated at second harmonic generation. The laser pulse energy was attenuated to around 40 mJ and focused onto the sample surface. The spot size is approximately 200 μm. A three-axis motorized translation stage was used for remote control of the sample position during data acquisition. The emission light was collected in standard atmospheric conditions and diverted through an optical fiber into a Czerny-Turner spectrometer (Horiba Jobin Yvon iHR 550) and an ICCD camera (Andor iStar 334 T). A LABVIEW-based data acquisition system was developed to provide proper timing between shutter and ICCD through a delay generator (Stanford DG645).

To calibrate the LIBS measurement, i.e., determine the relationship between intensity and concentration, we needed to create reliable standards with precisely known salt concentrations. We developed a procedure to repeatedly create salt films on metallic substrates. For this, we used a Perkin Mira-mist nebulizer, which allows us to create nanoscale droplets of salted solutions. We used it on room temperature samples and on substrates heated to ~500 K, the latter producing more consistent results. Heating allowed us to instantly dry the solution at contact with the substrate, creating a continuous film of salt. We used this procedure with a 100 times diluted 5 mol/L standard NaCl solution and with an artificial seawater solution from Lack Product Company LLC diluted to 0.198 g/L chlorine concentration. We created a series of $10 \times 10\,mm^2$ samples with 0.1, 0.3, 0.5, 0.8, and $1\,g/m^2$ chlorine concentrations. With this procedure, we obtained samples with high homogeneity and precisely known concentrations. SEM images of two samples with 0.3 and $0.8\,g/m^2$ chlorine concentrations are shown in Fig. 4.

On heated substrates, a continuous film of salt is observed on the surface of the samples. Although the salt is not observable,

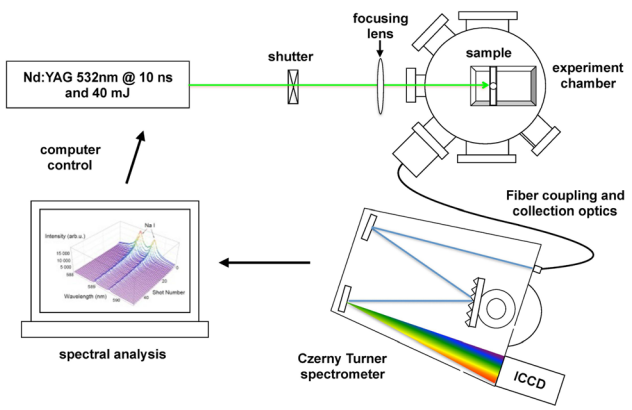

Fig. 3 Experimental setup for LIBS measurements

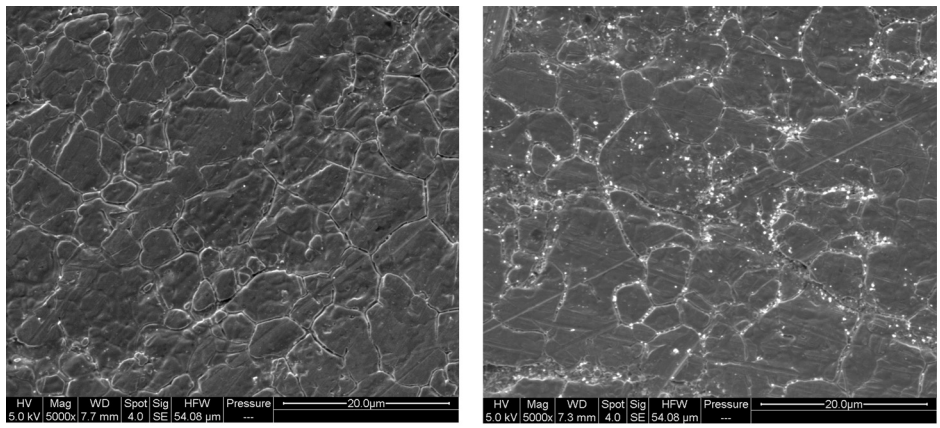

Fig. 4 Scanning electron micrographs of surfaces after salt deposition. Samples with 0.3 g/m^2 (left) and 0.8 g/m^2 (right) chlorine on stainless steel substrate (images taken using SEM X5000)

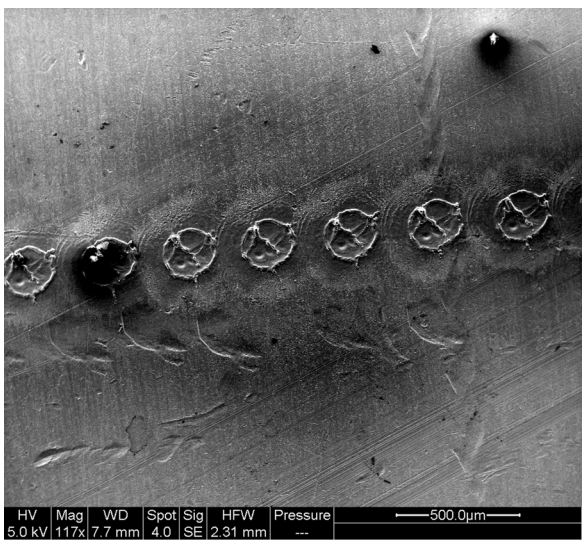

Fig. 5 LIBS laser photos (images taken using SEM X200)

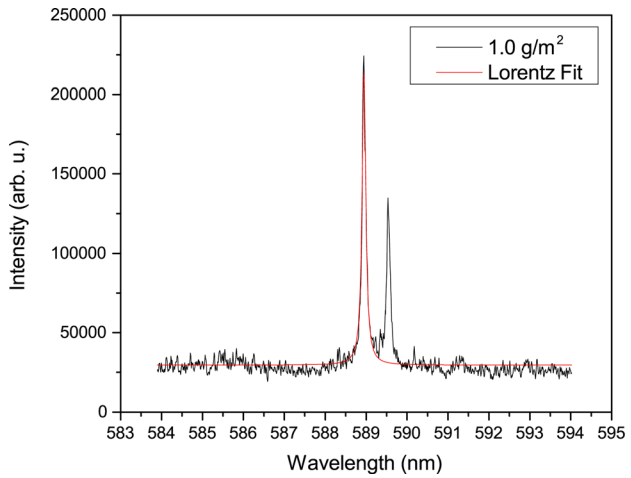

Fig. 6 NA I accumulated emission spectrum of NACL sample (1.0 g/m^2 chlorine) on SS and the Lorentz fit of 589.0 nm emission line

even at very high magnification, its presence, homogeneity, and relative salt concentrations were confirmed using EDS measurements. At concentrations higher than 0.5 g/m^2, crystal clusters of salt begin to appear, mainly gathering on crevices of the substrate. The salt layer also appears to be thick enough to smooth surface discontinuities of the substrate.

The LIBS laser shots present a high degree of geometrical reproducibility. Each shot creates two ventricles (see Fig. 5), corresponding to the laser beam profile. Laser shots are directly surrounded by a depletion area on which no salt is observed and by an affected area on which the high substrate temperature occurring during the shot causes the salt layer to melt. The diameter of the depletion area is approximately 0.5 mm. The thermally affected area depends on the substrate, and is 8 mm in diameter for stainless steel (SS) and 2 mm in diameter for aluminum. While the impact of the melting on the chlorine concentration is still not fully understood in our measurements, early observations suggest that there is little or no change for our concentrations of interest. This needs to be further investigated and confirmed.

The gate delay and the gate width time of the ICCD camera during the LIBS experiment were set to 1 μs and 0.25 μs, respectively, in order to avoid strong self-reversal of Na I emission lines. Five laser pulses were used at each location of the sample, obtaining a cumulative spectrum. Emission spectra obtained in this fashion at three different locations on the sample were used in the data analysis. A typical emission spectrum from a NaCl sample at a chlorine concentration of 1.0 g/m^2 is shown in Fig. 6. Two Na I emission lines at 589.0 nm and 589.6 nm are detected. The Na I emission line at 589.0 nm was fitted using a Lorentz distribution.

The dependence of the Na I line intensity on chlorine concentration is shown in Fig. 7. The integrated emission under the Lorentz-fit 589.0 nm line is plotted versus the chlorine concentration calculated using concentration of diluted NaCl solution, well-controlled flow of the nebulizer, and the spraying time on the substrates, and confirmed by SEM/EDS. Mean values of the Na I emission intensity are fitted to an exponential relationship, which is an approximate expression of the Lambert-Beer law [9]. This procedure allows us to account for self-absorption. The error bars of Na emission intensity are primarily due to large thermal-affected areas interfering with the results of the subsequent laser shots and the assumed Gaussian-shaped spraying distribution of the nebulizer. A good correlation of the measured intensity with the calculated concentration is found, suggesting that the measurement of Na can be a good surrogate for the measurement of salt concentration. Clearly, in order to use Na as a surrogate for Cl, it is necessary to show that, during transport and deposition, the Cl

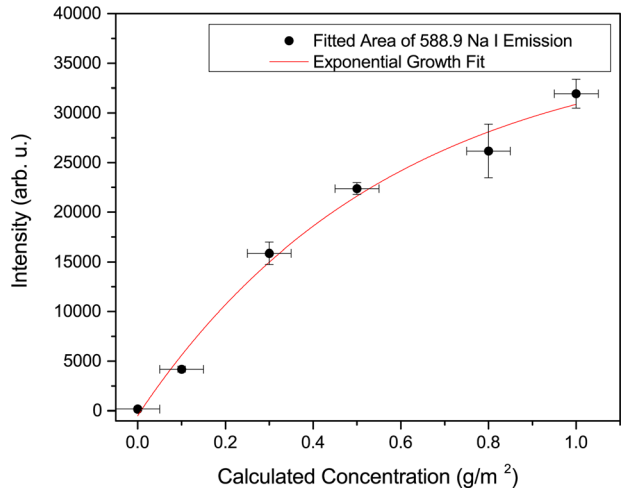

Fig. 7 Dependence of the NA I emission intensity on calculated chlorine concentration

and Na ratio remains approximately constant, as it is possible that environmental reactions during transport could cause this ratio to change. Finally, it is necessary to investigate other possible sources of Na (such as dust) that could generate a false positive signal. Nevertheless, the technique appears to be a promising path that allows the use of LIBS on steel while avoiding the concerns of the convolution of the Fe and Cl lines and permits low detection limits.

To summarize, sample-preparing procedures have been standardized in our experiment to create homogeneous salt deposits. The samples were analyzed by the LIBS system and the concentrations benchmarked by SEM/EDS. The ability to quantify Cl on stainless steel in the concentration of 0–1 g/m^2 has been investigated in this study by means of a surrogate Na measurement. For future work, synthetic seawater will be used to more realistically simulate the deposition on the canister. Other alkali metals such as Mg and K will be examined simultaneously with Na in the salt deposits for verification purposes. Fiber-coupled LIBS and coaxial focusing configuration will be developed to increase the flexibility of the LIBS system and to reduce the impact of misalignment of the focus. Experimental parameters (i.e., laser energy, gate width, and gate delay) will be optimized for this configuration. Calibration curves for these specific experimental parameters will be constructed, with a goal to develop a more general understanding, which would allow us to construct a universal calibration curve.

Sensing Stress Corrosion Cracks

Vertical axis cask systems (in particular HI-STORM) pose many geometric challenges for canister NDI. Figure 8 depicts an unwrapped overlay of canister welds on the overpack inner liner. The presence of guide channels limits access to portions of the bottom and circumferential welds. Furthermore, since the circumferential orientation of the canister relative to the overpack is unknown, the axial weld can either be exposed or inaccessible due to the guide channels. The limited accessibility associated with overpack guide channels excludes the use of conventional NDI methods based on point-by-point probing. Therefore, a noncontact-guided wave method is highly desirable for remote robotic delivery.

Rayleigh waves (surface waves), Lamb waves, and shear horizontal (SH) waves are well known types of guided waves commonly used for NDI [15]. Rayleigh waves propagate along a traction-free surface of a half-space. Lamb waves and SH waves propagate in a homogeneous isotropic traction-free plate. Because the guided waves are confined within boundaries or propagate along a boundary, they can travel a fairly long distance from a single probing position in a plate or pipe. This midrange volumetric

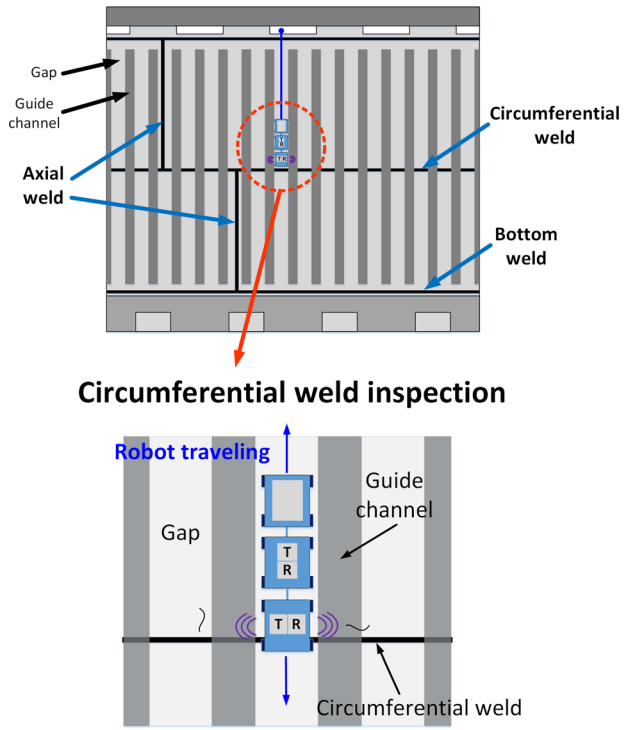

Fig. 8 Unwrapped overlay of canister welds on overpack inner liner with sensor car employing the pulse echo method

inspection capability is useful for applications with limited accessibility, as is the case for the canister.

Among the guided waves mentioned above, SH waves are chosen as the primary activation for canister NDI because they reflect from a crack oriented either normal or parallel to the wave vector. Lamb and Rayleigh waves have particle motions that are entirely in the sagittal plane determined by the wave vector and the plate thickness direction. Thus, they may not be sensitive to cracks that lie within that plane. On the other hand, SH waves have particle motion perpendicular to the sagittal plane. Hence, SH wave motion is essentially three-dimensional, which enables them to scatter and reflect from cracks aligned perpendicular or along the welds [16]. This reflection characteristic suggests that the pulse-echo method either along the weld as illustrated in Fig. 8, or normal to it, will be effective. Since the pulse-echo mode transmits and receives the wave at the same point, the number of transducer locations is minimized and the inspection method is simplified relative to through-transmission or pitch-catch. Moreover, the pulse-echo method assists in locating the welds by examining echoes from the weld-canister interfaces. This is important because visual identification of welds could be challenging since in some cases the welds are ground flush.

Initially, the SH_0 mode at 250 kHz has been selected for canister NDI from the dispersion curves shown in Fig. 9. The SH_0 mode is very attractive for midrange NDI because it is nondispersive, meaning that its phase velocity is independent of frequency. Additionally, it is equally sensitive to defects located anywhere across the plate thickness because the displacement profile is uniform. While excitation of a single mode is preferred from a signal processing standpoint, that would require use of a lower frequency, which would require a larger transducer and decrease defect resolution. The compromise solution is to excite the SH_0 mode at 250 kHz and accept that the SH_1 mode is likely to also be excited due to the source influence [15]. Fortunately, the SH_1 mode has a similar group velocity to the SH_0 mode, as well as good sensitivity to surface damage.

Compact EMATs are under development for canister NDI. The key requirements are that they be robot-deliverable and tolerant of

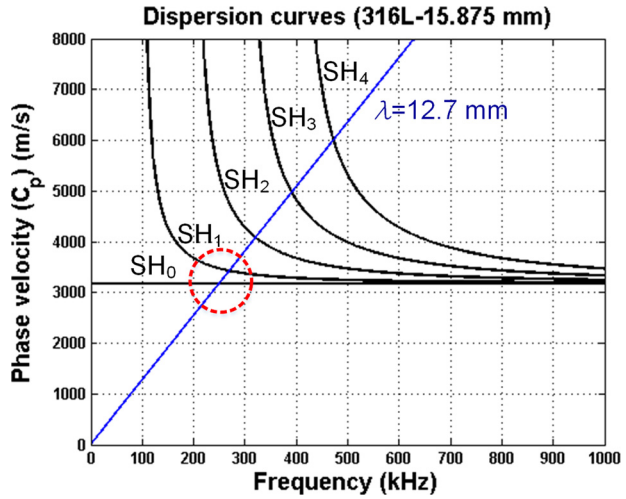

Fig. 9 SH wave dispersion curves for 15.9 mm thick stainless steel plate

high temperature and gamma radiation. Prototype EMATs are shown in Fig. 10, although it is not possible to see all of the components. The key components are a stack of permanent magnets, an electric coil, and a case. The outer dimensions are 70 mm × 44 mm × 19 mm (length × width × thickness), which fit into the sensor robot to be discussed later. As shown in Fig. 10, a pair of EMATs (transmitter and receiver) were arranged to examine echoes from notches in a 15.9 mm thick SS 304L plate. In one case, the notch is aligned with the wave vector so the echo is from the notch tips, and in the other case the notch is normal to the wave vector so the echo is from the notch face. A five-cycle sinusoidal signal of 1200 Vpp and 250 kHz from a RITEC RAM-5000 was applied to the transmitter and the receiver recorded wave signals with 30 dB gain that were postprocessed using MATLAB including a 500 kHz low-pass filter. Figure 11 depicts the corresponding A-scan signals. Though the baseline signal shows the existence of electromagnetic interference appearing at the beginning, the waveforms illustrate that SH waves can detect notches oriented at 0 and 90 deg to the wave vector. The notches are 19 mm long by 10 mm deep by 0.6 mm wide. The results shown are for notches located roughly 100 mm from the transmitter. It is worth noting that this is a first iteration result that we expect to be able to improve upon with further development.

Loretz force-based noncontact transduction depends on the liftoff distance between the EMAT and the substrate surface. Thus, to acquire consistent results, the robotic delivery system will be designed to maintain zero liftoff even though this is a noncontact method. Moreover, the EMATs will be positioned on the heat-affected zone, rather than on the weld cap itself in order to maintain zero liftoff. Note that in Fig. 10, the weld cap is nearly flush and the EMATs overlap the weld. Some canister welds are capped and some are ground flush, so for consistency EMATs will be positioned next to the weld rather than on it.

The pulse-echo methodology described above, and in more detail in Ref. [17], is intended for the detection of SCC, but nonlinear ultrasonics has enhanced potential for characterizing the extent of SCC once it has been detected. The length of branched cracks is difficult to accurately determine with linear ultrasonics and other NDI methods due to crack closure effects. But the nonlinearity associated with opening and closing of cracks is well-known to provide more accurate results and a variety of NDI methods have been developed to take advantage of the crack-induced tension-compression asymmetry [18–22]. The aim of this future work is to classify the cracks as 25, 50, or 75% through the wall thickness.

Robotic Delivery System

The interior cask environment presents many challenges to performing physical inspections and delivering sensors to locations of interest. Within the overpack, there is a limited amount of space for maneuvering to navigate the robotic delivery system. Additionally, the environmental conditions are particularly harsh for off-the-shelf robotic hardware due to high temperature and radiation. This section will discuss the methods for performing a robotic inspection and the design constraints imposed by the cask.

A typical vertical axis cask has cooling vents on the top (outlet) and bottom (inlet), and internal guide channels to maintain alignment of the multipurpose canister (MPC) housing spent nuclear fuel. Due to complex geometries at the bottom vent, the robotic delivery vehicle is designed to enter the cask through the outlet vent at the top of the cask, and from there gain access to the top of the MPC. Two methods are being considered to navigate across the top of the MPC: a delivery robot and a delivery arm, as depicted in Fig. 12. The use of a delivery robot provides greater maneuverability and is more self-contained than the arm when

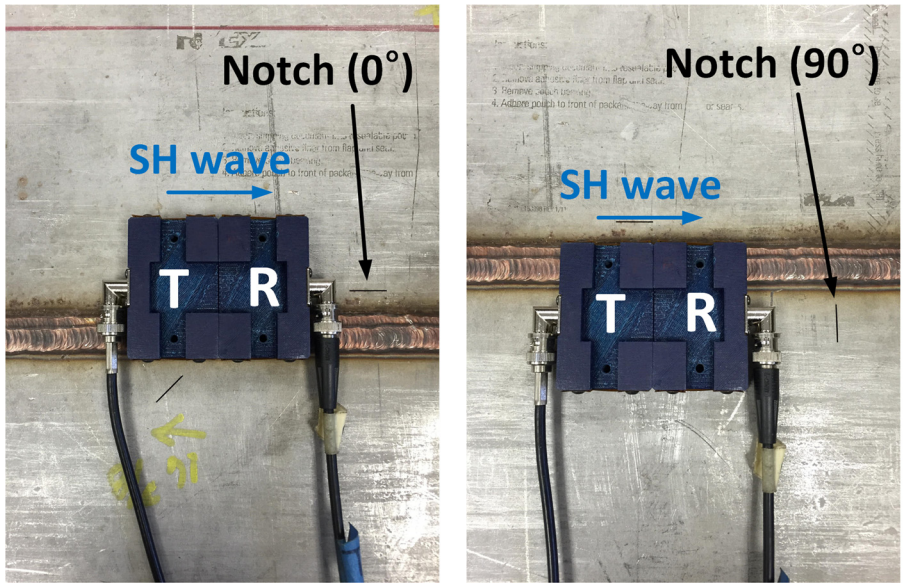

Fig. 10 EMAT arranged to detect notches oriented 0 deg (left) and 90 deg (right)

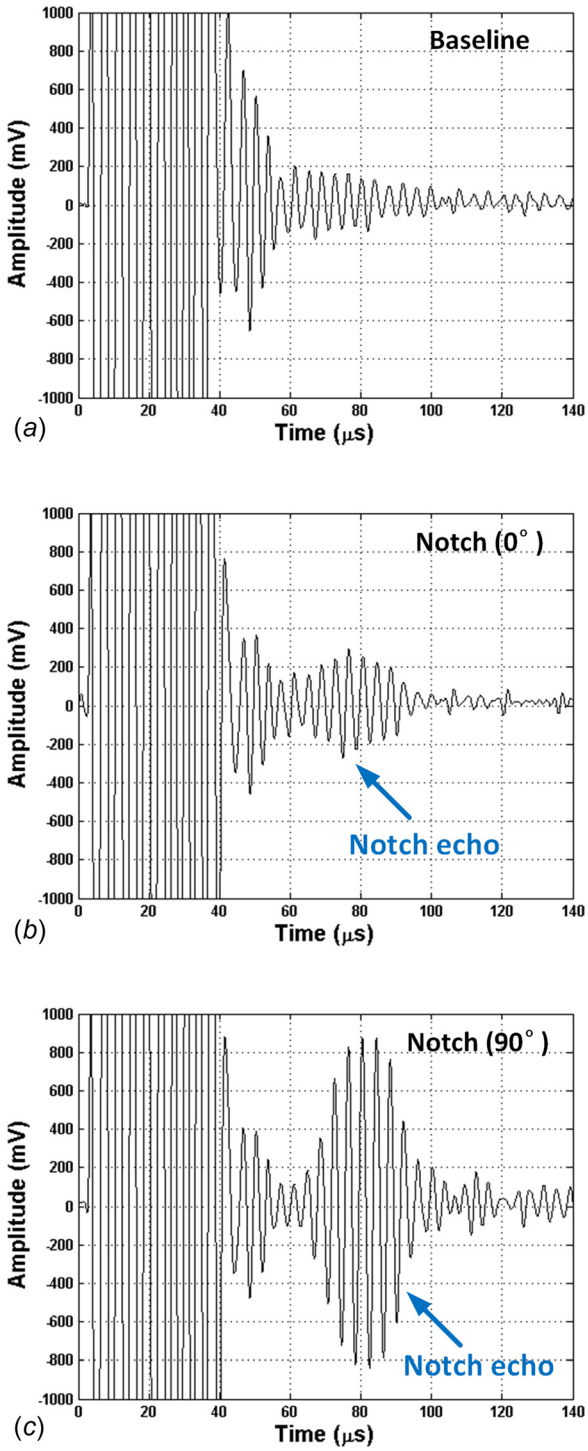

Fig. 11 A-Scan signals from EMAT arranged to detect notches oriented 0 deg and 90 deg

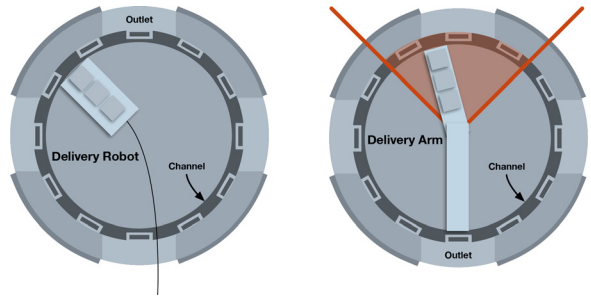

Fig. 12 The delivery robot and delivery arm are two methods for inserting the robot into the canister

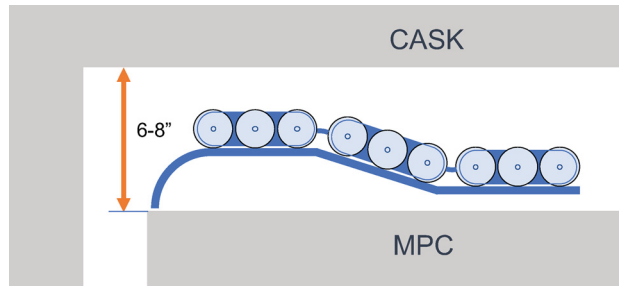

Fig. 13 The sensor robot will navigate over a curved platform to aid in insertion

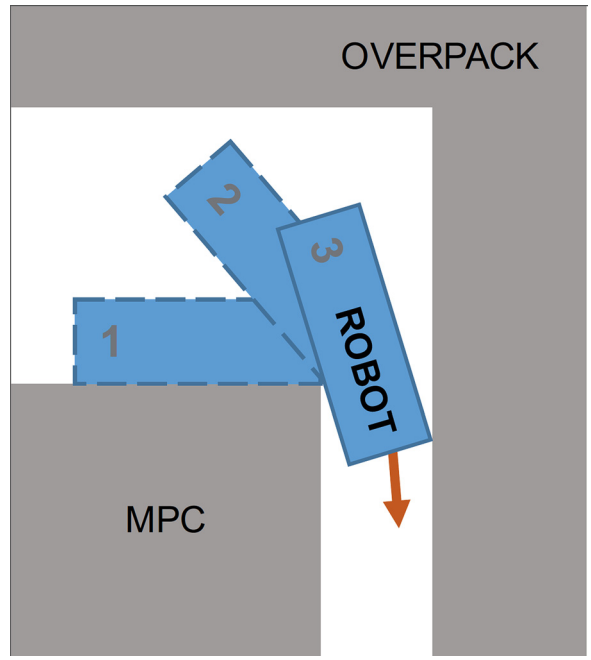

Fig. 14 Robot navigating around the edge of the MPC to access the guide channel gap

navigating on top of the MPC; however, the use of an actuated robot on the canister lid may provide more points of failure in terms of electronics and motors necessary to control the robot. The extension arm, while larger, could potentially be controlled using guide wires and pulleys that are actuated externally to the cask, resulting in a simple, fully passive device internal to the cask. To ensure that the extension arm can be easily retrieved, the pivot will be limited to a 45 deg angle and inserted into each of the outlet vents to ultimately provide a full 360 deg scanning region.

Once the delivery robot or delivery arm is positioned in front of a channel gap, a smaller "sensor robot" that contains sensors for inspection will be deployed into the channel gap. A curved entry surface (Fig. 13) is constructed on the delivery arm/robot to aid in the insertion of the sensor robot. The smaller "sensor robot" will actually consist of several connected cars, which improves access and permits proper distribution and spacing of sensors. This geometry also permits the addition of new or different sensors in the future, if necessary. The individual cars are connected to each other and to the command and control center by a tether or umbilical that distributes electrical power, optical signals, data, and cooling (discussed below), and provides a mechanical connection.

Navigating a robot in confined spaces can be a particularly difficult task. It is therefore imperative that once the delivery robot has entered the cask, the entire system can be passively retrieved in the event of a power failure. The geometry of the sensor robot is designed to ease the retrieval of the robot in these situations. As depicted in Fig. 14, the robot must navigate around the edge of the MPC to access the guide channel gap. This scenario is similar to what was known in many industrial assembly settings as a peg-in-hole problem.

The peg-in-hole analysis shows that insertion can result in jamming and/or wedging under certain geometric relationships between the inserted object and the entry space. The maximum geometric constraints of the robot can be determined by modeling the robot as a simplified, two-dimensional peg. Jamming refers to a scenario in which supporting forces become unbalanced and the robot becomes unable to enter the channel. Wedging occurs when the geometry of the robot is either under- or over-sized, potentially causing the robot to become immovable within the channel during either insertion or extraction. An optimal robot geometry is determined by analyzing the frictional constraint forces acting on the robot body. Further reading on this analysis can be found in Ref. [23].

Apart from mobility constraints, thermal constraints on the robot design are severe. The temperature on the outer surface of the MPC can surpass 177 °C (350 °F), which exceeds the operating range for most off-the-shelf robotics hardware. To regulate internal temperatures, cooled air will be circulated to components that require active cooling. Thermocouples will monitor these components to ensure that sufficient cooling is being provided. The tether or umbilical connecting the individual sensor robot units and the sensor robot to the command and control station will include the conduit for delivering cooling air to components requiring active cooling.

Throughout the inspection, the operator will be provided feedback of the exact location of the robot within the cask. One method to do this is through simultaneous localization and mapping (SLAM). The SLAM algorithm simultaneously determines the position of the robot while creating a map of the environment [24]. This process helps to pinpoint where a particular sensor measurement was obtained, as well as allowing repeatability when returning to a canister for future inspections. A particular difficulty in localizing the robot is the lack of unique features within the cask. The interior of a cask is a relatively sparse environment with symmetrical geometry, making it difficult to properly obtain the orientation of the robot within the cask. Additionally, the lack of sufficient lighting within the cask further diminishes the ability to accurately determine the position of the robot. To account for the low visibility, a light source will be added to the front of the robot. In future work, the components of the robotic inspection system will be tested for radiation tolerance at the Radiation Science and Engineering Center at Penn State.

Conclusion

A robotic inspection system is being designed for nondestructive inspection of dry storage canisters for spent nuclear fuel. The inspection system targets stress corrosion cracking for which two distinct sensing technologies are being developed: (1) LIBS to characterize salt deposits on the surface of the canister and (2) noncontact EMATs to generate shear horizontal waves that are sensitive to stress corrosion cracks. Both types of sensing systems will be delivered by a robot designed not to wedge or jam in the ventilation system during maneuvering, and to simultaneously perform localization and mapping in order to be able to return to measurement sites. To date, LIBS measurements have correlated Na I line intensity to Cl concentration and EMATs operating in pulse-echo mode with SH waves detected notches oriented both parallel and perpendicular to the wave vector. These results provide a good foundation for the robotic inspection system design, which is ongoing.

Acknowledgment

This material is based upon work performed under an Integrated Research Program by the DOE-Nuclear Energy Universities Program under Award No. DE-NE0008266.

References

[1] Song, H., and Popovics, J. S., 2016, "Hidden Disbond Detection in Spent Nuclear Fuel Storage Systems Using Air-Coupled Ultrasonics," SPIE Proceedings, **9803**, p. 980331.
[2] Tani, J., Mayazumi, M., and Hara, N., 2008, "Stress Corrosion Cracking of Stainless-Steel Canister for Concrete Cask Storage of Spent Fuel," J. Nucl. Mater., **379**(1–3), pp. 42–47.
[3] He, X., Mintz, T. S., Pabalan, R., Miller, L., and Oberson, G., 2014, "Assessment of Stress Corrosion Cracking Susceptibility for Austenitic Stainless Steels Exposed to Atmospheric Chloride and Non-Chloride Salts," United States Nuclear Regulatory Commision, Washington, DC, Report No. NUREG/CR-7170.
[4] Chu, S., 2013, "Failure Modes and Effects Analysis (FMEA) of Welded Stainless Steel Canisters for Dry Cask Storage Systems," Electric Power Research Institute, Palo Alto, CA, Report No. 3002000815.
[5] Hertzberg, R. W., 1996, *Deformation and Fracture Mechanics of Engineering Materials*, Wiley, New York.
[6] Enos, D. G., Bryan, C. R., and Norman, K. M., 2013, "Data Report on Corrosion Testing of Stainless Steel SNF Storage Canisters," Sandia National Laboratories, Report No. SAND2013-8314P.
[7] Caseres, L., Mintz, T. S., and Bayssie, M. M., 2010, "Atmospheric Stress Corrosion Cracking Susceptibility of Welded and Unwelded 304, 304L, and 316L Austenitic Stainless Steels Commonly Used for Dry Cask Storage Containers Exposed to Marine Environments," United States Nuclear Regulatory Commision, Washington, DC, Report No. NUREG/CR-7030.
[8] Eto, S., Tani, J., Shirai, K., and Fujii, T., 2013, "Measurement of Concentration of Chlorine Attached to a Stainless-Steel Canister Material Using Laser-Induced Breakdown Spectroscopy," Spectrochim. Acta B, **87**, pp. 74–80.
[9] Eto, S., and Fujii, T., 2015, "Laser-Induced Breakdown Spectroscopy System for Remote Measurement of Salt in a Narrow Gap," Spectrochim. Acta B, **116**, pp. 51–57.
[10] Radziemski, L. J., and Cremers, D. A., 2006, *Handbook of Laser Induced Breakdown Spectroscopy*, Wiley, New York.
[11] Hartig, K., Colgan, J., Kilcrease, D., Barefield, J., II, and Jovanovic, I., 2015, "Laser-Induced Breakdown Spectroscopy Using Mid-Infrared Femtosecond Pulses," J. Appl. Phys., **118**(4), p. 043107.
[12] Sugiyama, K., Fujii, T., Matsumura, T., Shiogama, Y., Yamaguchi, M., and Nemoto, K., 2010, "Detection of Chlorine With Concentration of 0.18 kg/m^3 in Concrete by Laser-Induced Breakdown Spectroscopy," Appl. Opt., **49**(13), pp. C181–C190.
[13] Culkin, F., and Cox, R., "Sodium, Potassium, Magnesium, Calcium and Strontium in Sea Water," *Deep Sea Research and Oceanographic Abstracts*, Vol. 13, Elsevier, Amsterdam, The Netherlands, pp. 789–804.
[14] Tan, M. M., Cui, S., Yoo, J., Han, S. H., Ham, K. S., Nam, S. H., and Lee, Y., 2012, "Feasibility of Laser-Induced Breakdown Spectroscopy (LIBS) for Classification of Sea Salts," Appl. Spectrosc., **66**(350), pp. 262–271.
[15] Rose, J. L., 2014, *Ultrasonic Guided Waves in Solid Media*, Cambridge University Press, Cambridge, UK.
[16] Ratassepp, M., Lowe, M. J. S., Cawley, P., and Klauson, A., 2008, "Scattering of the Fundamental Shear Horizontal Mode in a Plate When Incident at a Through Crack Aligned in the Propagation Direction of the Mode," J. Acoust. Soc. Am., **124**(5), pp. 2873–2882.
[17] Choi, S., Cho, H., Lindsey, M. S., and Lissenden, C. J., 2016, "Surface Crack Detection in Welded Stainless Steel Canisters Using Shear Horizontal Waves," ASME Paper No. PVP2016-63311.
[18] Zeitvogel, D. T., Matlack, K. H., Kim, J. Y., Jacobs, L. J., Singh, P. M., and Qu, J., 2014, "Characterization of Stress Corrosion Cracking in Carbon Steel Using Nonlinear Rayleigh Surface Waves," NDT&E Int., **62**, pp. 144–152.
[19] Morlock, F., 2014, "Evaluation of Stress Corrosion Cracking in Sensitized 304 Stainless Steel Using Nonlinear Rayleigh Waves," M.S. thesis, Georgia Tech, Atlanta, GA.
[20] Matlack, K. H., Kim, J. Y., Jacobs, L. J., and Qu, J., 2015, "Review of Second Harmonic Generation Measurement Techniques for Material State Determination in Metals," J. Nondestruct. Eval. **34**(1), pp. 1–23.
[21] Le Bas, P., Anderson, B. E., Remillieux, M., Pieczonka, L., and Ulrich, T. J., 2015, "Elasticity Nonlinear Diagnostic Method for Crack Detection and Depth Estimation," J. Acoust. Soc. Am., **138**(3), p. 1836.
[22] Chillara, V. K., and Lissenden, C. J., 2016, "Review of Nonlinear Ultrasonic Guided Wave Nondestructive Evaluation: Theory, Numerics and Experiments," Opt. Eng., **55**(1), p. 011002.
[23] McNelly, B., Leary, R., Brennan, S., and Reichard, K., 2016, "Characterizing Successful Robotic Insertion and Removal From a Dry Storage Cask Using Peg-Like Jamming and Wedging Analysis," ASME Paper No. PVP2016-63634.
[24] Levinson, J. S., and Thrun, S., 2010, "Robust Vehicle Localization in Urban Environments Using Probabilistic Maps," IEEE International Conference on Robotics and Automation (ICRA), Anchorage, AK, May 3–7, pp. 4372–4378.